Dalton Transactions

PAPER

View Article Online
View Journal | View Issue

Cite this: *Dalton Trans.*, 2014, **43**, 13683

Carbene based photochemical molecular assemblies for solar driven hydrogen generation†

Katrin Peuntinger,‡[a] T. David Pilz,‡[b,c] Robert Staehle,‡[b,d] Markus Schaub,[b,d] Simon Kaufhold,[d] Lydia Petermann,[d] Markus Wunderlin,[e] Helmar Görls,[c] Frank W. Heinemann,[b] Jing Li,[a] Thomas Drewello,[a] Johannes G. Vos,[f] Dirk M. Guldi*[a] and Sven Rau*[b,d]

Received 26th May 2014,
Accepted 29th July 2014

DOI: 10.1039/c4dt01546k

www.rsc.org/dalton

Novel photocatalysts based on ruthenium complexes with NHC (N-heterocyclic carbene)-type bridging ligands have been prepared and structurally and photophysically characterised. The identity of the NHC-unit of the bridging ligand was established unambiguously by means of X-ray structural analysis of a heterodinuclear ruthenium–silver complex. The photophysical data indicate ultrafast intersystem crossing into an emissive and a non-emissive triplet excited state after excitation of the ruthenium centre. Exceptionally high luminescence quantum yields of up to 39% and long lifetimes of up to 2 μs are some of the triplet excited state characteristics. Preliminary studies into the visible light driven photocatalytic hydrogen formation show no induction phase and constant turnover frequencies that are independent on the concentration of the photocatalyst. In conclusion this supports the notion of a stable assembly under photocatalytic conditions.

Introduction

The identification of novel technologies capable of producing energy in a sustainable manner has become an important research aim to control the ever increasing need for energy and the resulting climate change. In this context, light driven water cleavage with formation of hydrogen represents a promising approach.[1] Different photocatalytic concepts were developed in the past, using, for instance, heterogeneous photocenters, photo-electrochemical cells,[2] and intermolecular systems.[3–6] Most recently, intramolecular systems were developed, consisting of a photosensitiser, a catalytically active site, and a bridging ligand.[3–7] Such a molecular design, first realised in 2006,[8] powers an intramolecular electron transfer from the chromophore towards the catalyst *via* a bridging ligand during the lifetime of the MLCT (metal to ligand charge transfer)-excited state.[9] Thus, we recently reported that in such a photocatalyst – $[(tbbpy)_2Ru(\mu\text{-}tpphz)\{PdCl_2\}](PF_6)_2$ (**tbbpy** = 4,4′-*tert*-butyl-2,2′bipyridine and tpphz = tetrapyrido[3,2-*a*:2′,3′-*c*:3″,2″-*h*:2‴,3‴-*j*]phenazine) – photoreduction of the palladium centre precedes the production of hydrogen.[9] Upon regeneration of the chromophore, protons are reduced to hydrogen at catalytic centre in moderate turnovers.

This modular concept allows for a rational design and for the systematic optimization of the individual subunits. This is of significance for the development of new types of catalysts, which may overcome the drawbacks of the previous generations. Importantly, for the advancement of intramolecular systems several design considerations have to be taken into account.[10] The photochemical properties as well as the redox properties of the photoexcited state have to allow the reduction of appropriate catalytic centres and these reduced centres must be capable of reducing the substrate, *i.e.* protons to hydrogen. This ability correlates also with the structure of the catalytic centre. In particular, the excited state energy of the

[a]*Friedrich-Alexander-Universität Erlangen-Nürnberg, Department of Chemistry and Pharmacy and Interdisciplinary Center for Molecular Materials (ICMM), Egerlandstrasse 3, 91058 Erlangen, Germany. E-mail: dirk.guldi@chemie.uni-erlangen.de; Fax: (+49) 9131-852-8307*
[b]*Friedrich-Alexander-Universität Erlangen-Nürnberg, Department Chemie und Pharmazie, Egerlandstrasse 1, 91058 Erlangen, Germany*
[c]*Institut für Anorganische und Analytische Chemie, Friedrich-Schiller-Universität Jena, August-Bebel-Strasse 2, 07743 Jena, Germany*
[d]*Institut für Anorganische Chemie I, Universität Ulm, Albert-Einstein-Allee 11, 89081 Ulm, Germany. E-mail: sven.rau@uni-ulm.de; Fax: (+49) 731/50-23039; Tel: (+49) 731/50-22575*
[e]*Institut für Organische Chemie II und Neue Materialien, Universität Ulm, Albert-Einstein-Allee 11, 89081 Ulm, Germany*
[f]*SRC for Solar Energy Conversion School of Chemical Sciences, Dublin City University, Dublin 9, Ireland*

†Electronic supplementary information (ESI) available: Synthesis, crystal data, NMR H/D exchange, mass spectrometry, electrochemistry, spectroelectrochemistry, and photophysical data. CCDC 893729–893733, 765499 and 796734. For ESI and crystallographic data in CIF or other electronic format see DOI: 10.1039/c4dt01546k

‡K.P. and T.D.P. and R.S. contributed equally to the manuscript.

chromophore should be tuneable and the bridging ligand should be electronically linked in a stable manner to the catalytic centre in all of its redox states leading to chemically stable compounds. The later point has been emphasized by Hammarström *et al.* for a dinuclear ruthenium–palladium catalyst.[11] During photocatalysis, palladium colloids were detected, which implies their release from the reduced complex in the weakly stabilizing NN-chelating environment. Moreover, the ensuing investigations on platinum catalysts based on polypyridine ligands showed contradicting results. Eisenberg *et al.* could detect a photodecomposition of platinum catalysts, which led to the conclusion that the resulting colloids may serve as active catalysts.[12] However, in contrast to this findings, Sakai *et al.* demonstrated that some of his platinum catalysts are stable.[13] Consequently, the question, under which circumstances colloids are formed and whether they are the catalytically active species, cannot be answered satisfyingly yet for oligopyridine based palladium or platinum catalysts. It is therefore highly desirable to take alternative bridging ligands with more suitable donor sets into consideration. The problem of stability of the low valence state of a catalyst is addressed in great detail in organometallic catalysis. Hence, appropriate ligands such as phosphine and, more recently, NHC ligands have been favoured. Research in this area is increasing rapidly, showing the importance and advantages of these systems, in particular, the enhanced stability. Therefore, these NHC ligands are useful in gaining full control over the electronic and steric properties of the catalytic centre during particular reactions.[14] Recently, Chung *et al.* showed, for instance, that a dinuclear (NHC)-ruthenium–iridium-complex can be used as a sensitizer for CO.[15]

Motivated by these observations, we present here the synthesis and characterisation of the first photocatalyst for the water reduction containing a NHC-NN-bridging ligand[15–17] based on 1,3-(bisbenzyl)-1*H*-imidazo[4,5-*f*][1,10]phenanthrolinium **bbip**$^+$. Starting from **[Ru(bbip)]**$^{3+}$ [(tbbpy)$_2$Ru(bbip)](PF$_6$)$_3$ as a building block the heterometallic intramolecular photocatalysts [(tbbpy)$_2$Ru(μ-bbip){AgCl}]Cl$_2$ (**[Ru(bbip)Ag]**$^{2+}$), [(tbbpy)$_2$Ru(μ-bbip){PdCl$_2$X}]Cl$_2$ (X = coordinated solvent; **[Ru(bbip)Pd]**$^{2+}$), and [(tbbpy)$_2$Ru(μ-bbip){Rh(cod)Cl}]Cl$_2$ (cod = 1,5-cyclooctadiene; **[Ru(bbip)Rh]**$^{2+}$) were prepared. A detailed structural and photophysical investigation corroborates photoinduced electron transfer reactions that are the key step for the overall photocatalytic activity.

Results and discussion

Synthesis of the ligands

1*H*-Imidazo[4,5-*f*][1,10]phenanthroline (**ip**) was synthesised according to literature[18] and used as starting material for the synthesis of the NN-NHC-ligand **bbip**$^+$ by stepwise alkylation with benzyl bromide (Fig. 1; for detailed synthesis see ESI†). The successful formation of the compounds was verified by NMR. The typical imidazolium salt properties of **bbip**$^+$ were revealed in a kinetic NMR experiment. In particular, **bbip**$^+$ shows in methanol-d_4 fast H/D-exchange of the active 2-ip proton (Fig. S2†). A first order decay of the relative peak area of the NC*H*N-proton was observed with a rate constant of $k_{H/D}$ = 2.36 ± 0.01 × 10^{-5} s^{-1} ($t_{1/2}$ = 490 ± 2 minutes at 25 °C).

The formation of all ligands was further verified by ESI-HRMS, elemental analysis and X-ray crystallography (see ESI†). Selected bond lengths and angles are listed in Table 1. A detailed discussion is given below.

Synthesis of the NN-chelated Ru complexes

To probe and compare the coordinating features of the potential bridging ligands a series of new ruthenium complexes was prepared as depicted in Fig. 2 (for details regarding synthesis see ESI†).

Ruthenium was chosen because of its favourable light harvesting properties. The syntheses of the ruthenium complexes were carried out by the reaction of stoichiometric reactions of [Ru(tbbpy)$_2$Cl$_2$] and **ip**, **bip**, or **bbip**$^+$, in ethanol–water using a microwave reactor. After counter ion exchange with NH_4PF_6, [Ru(tbbpy)$_2$(ip)][PF$_6$]$_2$ (**[Ru(ip)]**$^{2+}$), [Ru(tbbpy)$_2$(bip)][PF$_6$]$_2$ (**[Ru(bip)]**$^{2+}$), and **[Ru(bbip)]**$^{3+}$ were obtained in good yields. In the case of **[Ru(bbip)]**$^{3+}$, a slightly longer reaction time of five hours was necessary to drive the reaction between the positively charged ruthenium and the positively charged ligand. Chromatographic purification yielded pure **[Ru(ip)]**$^{2+}$, **[Ru(bip)]**$^{2+}$, and **[Ru(bbip)]**$^{3+}$ (for details regarding the synthesis see ESI†). ^{1}H- and ^{13}C-NMR spectroscopy revealed the typical imidazolium salt properties of **[Ru(bbip)]**$^{3+}$, while the H/D-exchange in methanol-d_4 was too fast for kinetic NMR-investigations (compared to **bbip**$^+$, Fig. S2†). Most important is the pattern of the phenanthroline related 6/9-, 5/10- and 4/11-proton signals, which implies the presence of a symmetric ligand in the case of **[Ru(ip)]**$^{2+}$ and **[Ru(bbip)]**$^{3+}$ and an asym-

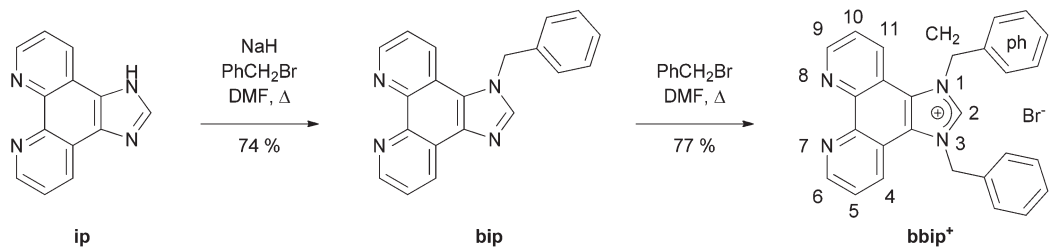

Fig. 1 Stepwise synthesis of **bbip**$^+$ starting from **ip**.

Table 1 Selected bond lengths and angles of the imidazole-moiety and the NN-coordination sphere of the ligands **ip**, **bip**, and **bbip**$^+$ and of the resulting ruthenium complexes **[Ru(ip)]**$^{2+}$, **[Ru(bip)]**$^{2+}$, **[Ru(bbip)]**$^{3+}$, and **[Ru(bbip)Ag]**$^{2+}$ (numbering refers to Fig. 6)

Bond lengths [Å]	**ip**[a]	**bip**	**bbip**$^+$	**[Ru(ip)]**$^{2+}$	**[Ru(bip)]**$^{2+}$	**[Ru(bbip)]**$^{3+}$	**[Ru(bbip)Ag]**$^{2+}$
Ag1–C13	—	—	—	—	—	—	2.080 (6)
Ag1–Cl1	—	—	—	—	—	—	2.3214 (16)
Ru1–N1	—	—	—	2.060 (4)	2.064 (5)	2.057 (4)	2.055 (5)
Ru1–N2	—	—	—	2.058 (4)	2.055 (4)	2.056 (4)	2.067 (5)
N3–C13	1.330 (4)	1.357 (2)	1.330 (9)	1.336 (8)	1.308 (7)	1.318 (7)	1.357 (9)
N4–C13	1.331 (4)	1.315 (3)	1.322 (8)	1.338 (8)	1.368 (7)	1.323 (7)	1.357 (9)
N3–C5	1.392 (3)	1.391 (2)	1.400 (8)	1.361 (7)	1.376 (7)	1.395 (7)	1.395 (7)
N4–C6	1.391 (3)	1.387 (2)	1.391 (9)	1.376 (7)	1.376 (7)	1.395 (7)	1.386 (7)
C5–C6	1.365 (4)	1.378 (3)	1.386 (9)	1.373 (8)	1.379 (8)	1.380 (8)	1.379 (9)
N1–C12	1.356 (3)	1.352 (2)	1.367 (9)	1.367 (7)	1.372 (7)	1.363 (7)	1.373 (7)
N2–C11	1.360 (3)	1.357 (2)	1.358 (8)	1.385 (7)	1.364 (8)	1.375 (7)	1.372 (7)
C11–C12	1.468 (4)	1.463 (3)	1.454 (10)	1.443 (8)	1.421 (8)	1.449 (7)	1.442 (9)
Angles [°]	**ip**[a]	**Bip**	**bbip**$^+$	**[Ru(ip)]**$^{2+}$	**[Ru(bip)]**$^{2+}$	**[Ru(bbip)]**$^{3+}$	**[Ru(bbip)Ag]**$^{2+}$
C13–Ag1–Cl1	—	—	—	—	—	—	178.9 (2)
N1–Ru1–N2	—	—	—	80.15 (17)	79.43 (17)	79.18 (16)	79.32 (19)
N3–C13–N4	110.1 (2)	113.60 (16)	110.9 (6)	112.5 (5)	113.5 (5)	111.0 (5)	105.7 (5)
C13–N3–C5	107.9 (2)	106.09 (16)	108.1 (6)	107.5 (5)	105.9 (5)	107.8 (5)	110.6 (5)
C13–N4–C6	107.8 (2)	104.28 (16)	107.7 (6)	103.7 (5)	104.1 (5)	107.9 (5)	111.0 (5)
N3–C5–C6	106.9 (2)	105.47 (15)	105.8 (6)	105.5 (5)	105.4 (5)	106.6 (5)	106.4 (5)
C5–C6–N4	107.2 (2)	110.56 (16)	107.5 (6)	110.7 (5)	111.1 (5)	106.6 (5)	106.4 (5)
N1–C12–C11	117.7 (2)	116.59 (15)	116.2 (6)	116.3 (5)	115.1 (5)	115.8 (5)	116.0 (5)
N2–C11–C12	117.0 (2)	117.03 (16)	116.5 (6)	115.8 (5)	117.4 (5)	114.9 (5)	115.3 (5)

[a] Refers to the protonated **ip**.

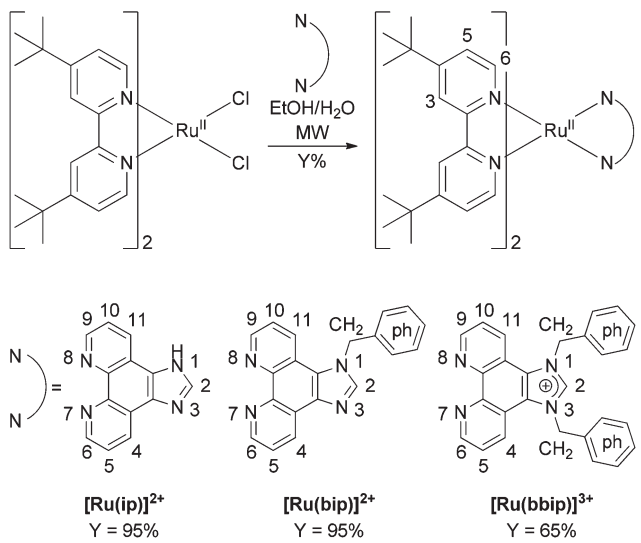

Fig. 2 General synthesis of ruthenium complexes with ip-type ligands.

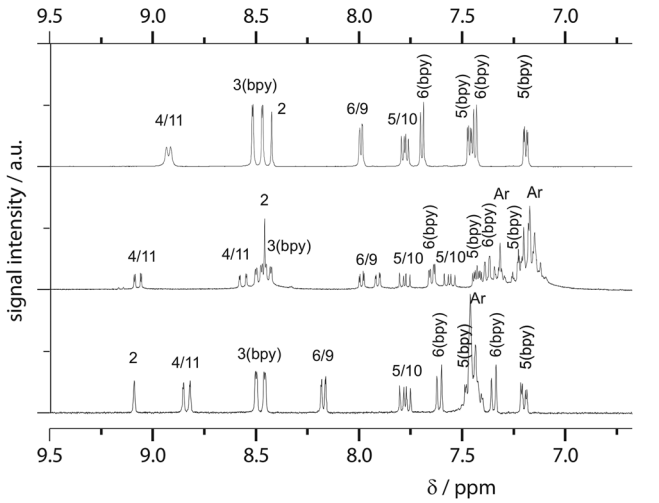

Fig. 3 Aromatic region of the ^{1}H-NMR spectra for **[Ru(ip)]**$^{2+}$ (top), **[Ru(bip)]**$^{2+}$ (middle) and **[Ru(bbip)]**$^{3+}$ (bottom) in acetonitrile-d_3 with corresponding peak assignment.

metry ligand in the case of **[Ru(bip)]**$^{2+}$ (Fig. 3; for numbering see Fig. 2).

The benzylic CH-signals further corroborate these observations ($\delta_{\mathbf{Ru(bip)}}4H_{CH_2}$ = 5.99 ppm and $\delta_{\mathbf{Ru(bbip)}}4H_{CH_2}$ = 6.17 ppm). Significant is also the shift of the singlet signals of the 2-protons due to the +I-effect ($\delta_{\mathbf{Ru(ip)}}H_{2\text{-ip}}$ = 8.44 ppm, $\delta_{\mathbf{Ru(bip)}}H_{2\text{-ip}}$ = 8.48 ppm, and $\delta_{\mathbf{Ru(bbip)}}H_{2\text{-ip}}$ = 9.08 ppm) due to increasing deshielding of the NC*H*N-proton after stepwise alkylation and salt formation (**[Ru(bbip)]**$^{3+}$).

ESI-HRMS mass spectrometry and elemental analysis further confirm the formation of the complexes. Suitable crystals for X-ray crystallography were obtained for all of the monometallic ruthenium complexes (Table 1 and ESI†). A detailed discussion is given below.

Synthesis of [Ru(bbip)Ag]$^{2+}$

At this point, transformation of the imidazolium salt into the corresponding carbene derivatives to synthesise the corres-

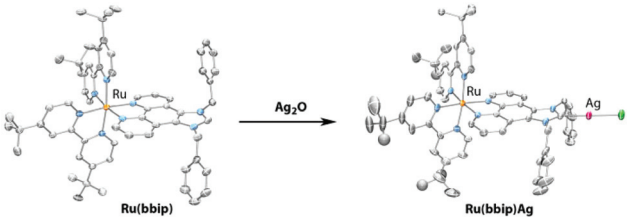

Fig. 4 Synthesis of $[Ru(bbip)Ag]^{2+}$ from $[Ru(bbip)]^{3+}$. Displayed are the crystal structures of both complexes; counter ions, solvent molecules, and protons are omitted for clarity.

ponding NHC-metal complexes proved to be the most challenging step and a number of different methods were attempted to prepare metal-NHC complexes.[19] They include isolation of the free carbene, followed by subsequent complexation to an coordinatively unsaturated metal fragment, cleavage of the tetraaminoethene derivatives with suitable metal precursors, preparation of a carbene transfer agent for transmetalation, and synthesis of the NHC-ligand at the metal center.[20–24] Surprisingly the target compound $[Ru(bbip)Ag]^{2+}$ could only be obtained by reacting the chloride salt of $[Ru(bbip)]^{3+}$ with Ag_2O in dry dichloromethane. This resulted in the transformation of the imidazolium salt structure into the required NHC unit (Fig. 4; for details regarding the synthesis see ESI†).

The presence of the NHC unit was corroborated by the loss of the H2 signal in the ^{1}H-NMR and the typical high field shift of the C2 signal (146.82→199.72 ppm) in the ^{13}C-NMR, the X-ray crystal structure confirm the successful NHC formation (Fig. 4, Table 1 and ESI†) and by ESI-HRMS analyses of $[Ru(bbip)Ag]^{2+}$ (see ESI†).

As the first fully characterised bbip-carbene complex, $[Ru(bbip)Ag]^{2+}$ was subject of detailed investigations into its fragmentation behaviour under MS and MS/MS conditions, using ESI as the ionisation method.

A 1 mM MeOH solution of $[Ru(bbip)Ag]^{2+}$ ($[[(tbbpy)_2Ru(\mu\text{-}bbip)AgCl]Cl_2$) was electrosprayed and the resulting MS spectrum is depicted in Fig. 5a (top trace). The most abundant ion corresponds to the singly charged $[Ru(bbip)Ag]^{2+}[Cl]^-$ ($[[(tbbpy)_2Ru(\mu\text{-}bbip)AgCl]Cl]^+$) ion ($m/z$ = 1216.8), which represents the quasi-molecular ion, the identity of which has been verified by its isotope pattern and by ESI-HRMS. Interestingly, there are additional signals for $[Ru(bbip)Ag]^{2+}$ at m/z = 591.1 and $[Ru(bbip)]^{2+}$ at m/z = 519.2 (Fig. 5 and S3†). Since we have no other indications of impurities present in the sample, these fragments most probably originate from dissociations occurring during the electrospray process of the sample. The ESI-MS (Fig. 5a) differs from the MS/MS (Fig. 5b), which is not unusual since the ESI-MS may result from a multitude of processes occurring in the spray, while the MS/MS reveals the true fragmentation behaviour of a selected precursor ion.

In the MS/MS experiment, the $[Ru(bbip)Ag]^{2+}[Cl]^-$ ion was selected and submitted to collision-induced dissociations (CID) using helium as the collision gas. The resulting daughter ion spectrum is shown in Fig. 5b.

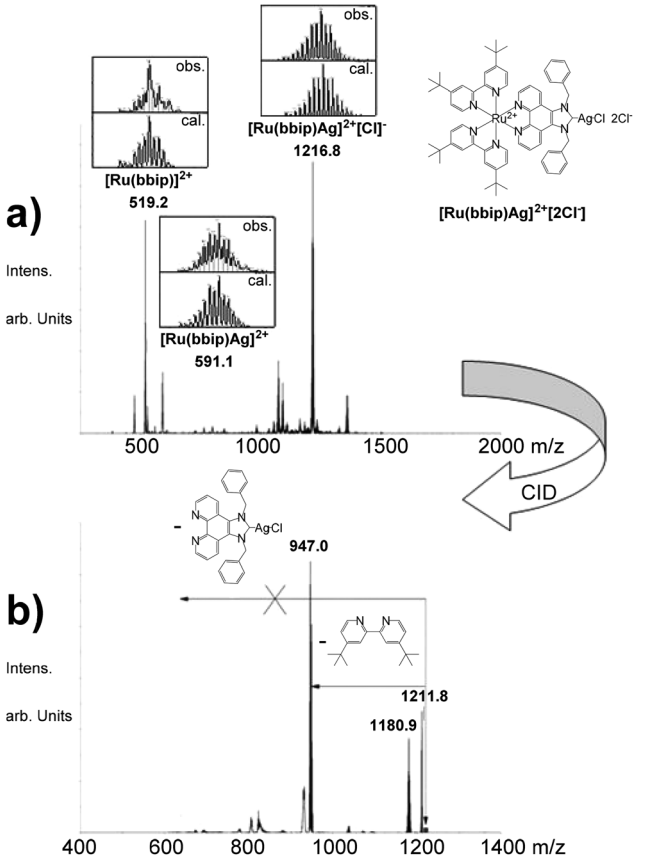

Fig. 5 (a) MS spectrum of $[Ru(bbip)Ag]^{2+}$. (b) MS^2 spectrum of m/z = 1217, which shows the $[Ru(bbip)Ag]^{2+}[Cl]^-$ cation.

As far as the fragmentation pattern is concerned, a statistical loss of the **tbbpy** *versus* **bbip**$^+$ ligand would lead to a 2 : 1 ratio of the respective signals. However, the loss of the **bbip**$^+$ ligand is virtually absent from the MS/MS spectrum and only loss of the tbbpy ligand is observed as shown in Fig. 5b. This indicates a much stronger bond between **bbip**$^+$ and ruthenium compared to **tbbpy**. Similar findings were reported in earlier investigations related to the competitive complexation of 1,10-phenanthroline (**phen**) and 2,2′-bipyridine (**bpy**) to Mn^{2+} ions.[25] In this study, **bpy** replaces **tbbpy**, and **phen** replaces **bbip**$^+$. The weaker complexation of **bpy** ligands by Mn^{2+} was attributed to its higher flexibility.[25] While **phen** is frozen in the *cis* configuration, **bpy** has the ability to rotate into the *trans* form which may lead to monodentate coordination of the ligands, followed by ligand loss as has also been observed in photochemical experiments with ruthenium polypyridyl complexes. This aspect might be even more relevant for **tbbpy** with its two *tert*-butyl groups.

It is interesting to note, that the fragmentation of $[Ru(bbip)Ag]^{2+}$ under ESI-MS conditions (Fig. 5a) leads to the dication $[Ru(bbip)]^{2+}$ (m/z = 519.23), an ion that most probably contains a free carbene structure within the imidazolium unit. The formation of imidazolium-based carbenes is not unexpected under ESI-MS conditions, but the resulting carbene is in most cases a neutral species and such reactions cannot be

followed by mass spectrometry which relies on the detection of ions. However, in the present case the reaction product can be detected as the ligand is firmly attached to the charge-carrying central metal cation, which acts as a charge tag for the free carbene.[26,27] This analysis provides the firm basis for the characterization of further and more complex μ-bbip bridged complexes by mass spectroscopy. However, the ease by which fragmentation can occur, allows that only imprecise predictions can be made of the actual stability of these compounds.

Structural analysis

With the X-ray structures of the free ligands (**ip**, **bip**, **bbip**$^+$), the corresponding ruthenium complexes ([**Ru(ip)**]$^{2+}$, [**Ru(bip)**]$^{2+}$, [**Ru(bbip)**]$^{3+}$), and the heterometallic complex ([**Ru(bbip)Ag**]$^{2+}$) in hand a detailed structural comparison is possible (Fig. 4 and ESI†). Important distances and angles are summarized in Table 1 (numbering refers to Fig. 6).

All distances and angles are in good agreement compared to similar compounds.[15,16,28–30] No or only small changes of the bond distances (N1–C12, N2–C11, C11–C12) and bond angles (N1–C12–C11, N2–C11–C12) in the phenanthroline part are observed between the free ligands and their corresponding metal complexes. The phenanthroline part remains also widely unaffected by changes at the imidazole part with respect to bond lengths and bond angles within the series of the free ligands and the corresponding complexes. In contrast, the imidazole part changes with the stepwise introduction of benzyl moieties. Although, the imidazole rings exhibit almost identical N3–C5, N4–C6, and C5–C6 bond lengths, a significant asymmetry by means of shortening and elongating of the N4–C13 and N3–C13 bond is discernable in **bip** and [**Ru(bip)**]$^{2+}$. This is attributed to the partial double bond character of N4–C13 (**bip**) and N4–C13 ([**Ru(bip)**]$^{2+}$). Various twist angles regarding the benzyl groups were found, which are, however, due to crystal packing distortions and indicate a free rotation in solution, which is in good agreement with ^{1}H-NMR experiments (*e.g.* singlet for the benzylic CH_2 group; see ESI†). The Ag1–C13 (2.080(6) Å) and Ag1–Cl1 (2.3214(16) Å) bond distances are in good agreement with the expected values for [(NHC)AgCl]-type complexes. The bond angle C13–Ag1–Cl1 (178.9(2)°) is almost linear and no indications for other coordination geometries were observed, which are known for [(NHC)-AgX]-type complexes (X = Cl, Br, I).[31–33]

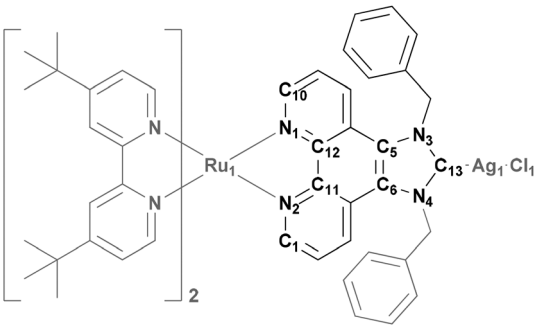

Fig. 6 Numbering of the atoms in Table 1.

Synthesis of [Ru(bbip)Pd]$^{2+}$ and [Ru(bbip)Rh]$^{2+}$

Next, **bbip**$^+$ was tested as bridging ligand to different catalytically active metals. In this context, the main advantage of silver carbene complexes is that they enable the transfer of coordinated NHC ligands to almost any kind of metal centre in transmetalation reactions.[23,34–36] The resulting assemblies are potentially capable of photoinduced intramolecular electron or energy transfer between the photosensitiser and the catalytically active site across the bridging ligand. It is also reasonable to expect photocatalytic activity and even more important a more stable binding of the catalytic active metal during catalytic activity.

By reacting [**Ru(bbip)Ag**]$^{2+}$ with $Pd(CH_3CN)_2Cl_2$ in dichloromethane (Fig. 7) an insoluble AgCl-precipitate was formed. From this observation we infer the formation of the palladium-NHC complex [**Ru(bbip)Pd**]$^{2+}$. The removal of the precipitate and the evaporation of the remaining solvent yielded [**Ru(bbip)Pd**]$^{2+}$. The corresponding rhodium complex was synthesized analogously (for details regarding the synthesis see ESI†). The formation of the target compound was confirmed by means of ^{1}H-NMR- and ESI-HRMS experiments (Fig. 8 and ESI†). The splitting of the CH_2-signals ($\delta_{\mathbf{Ru(bbip)Pd}}H_{CH_2}$ = 7.14 ppm (d, J =

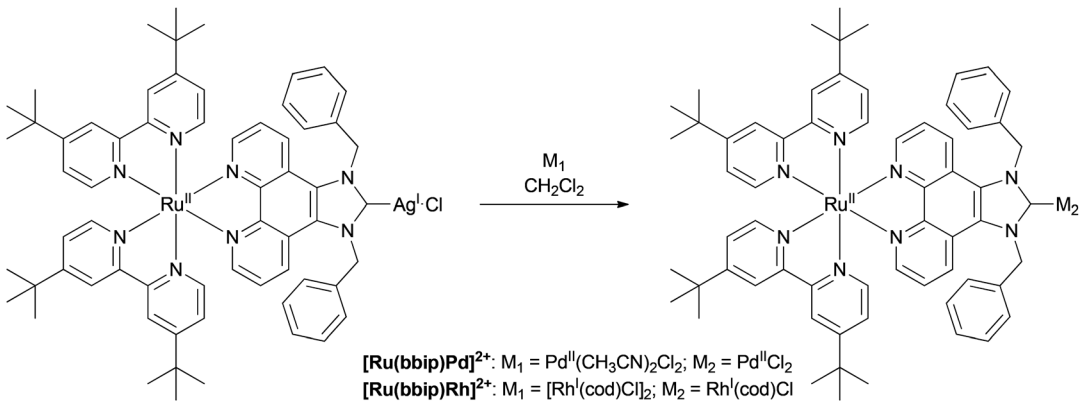

Fig. 7 Synthesis of [Ru(bbip)Pd]$^{2+}$ and [Ru(bbip)Rh]$^{2+}$.

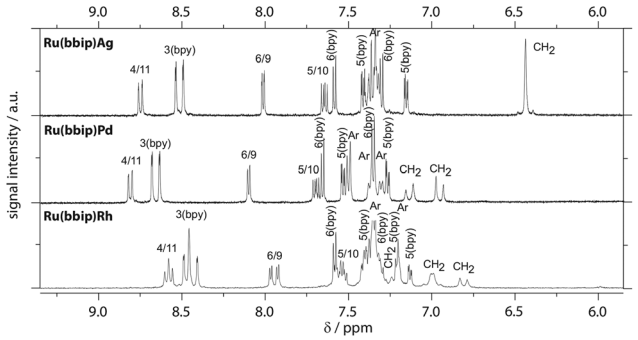

Fig. 8 Aromatic region of the ^{1}H-NMR-spectra of $[Ru(bbip)Ag]^{2+}$, $[Ru(bbip)Pd]^{2+}$, and $[Ru(bbip)Rh]^{2+}$ in acetonitrile-d_3 with signal assignments.

17.7 Hz) and 6.96 ppm (d, J = 17.6 Hz) of $[Ru(bbip)Pd]^{2+}$ into two sets may be interpreted in two ways. Firstly, a dimeric complex $[[Ru(bbip)Pd]_2]^{4+}$ may be formed in solution.[37] Secondly, the splitting could be caused by hindered rotation of the benzyl groups[38] at room temperature. Similar effects could be seen for $[Ru(bbip)Rh]^{2+}$.

Electrochemistry

Electrochemical characterisation of $[Ru(bbip)]^{3+}$ and $[Ru(bbip)Ag]^{2+}$ reveals that in these novel NN-NHC complexes the basic features of $[Ru(bpy)_3]^{2+}$ are maintained. In particular, all of the complexes show three ligand centred reductions and one metal centred oxidation (Fig. S4,† and Table 2). Comparing the data obtained with a structurally related $[Ru(tbbpy)_2(phen)]^{2+}$ reference shows that the potential for the first reduction of $[Ru(bbip)]^{3+}$ and $[Ru(bbip)Ag]^{2+}$ is more positive and the oxidation of the ruthenium centre appears also at slightly more positive potentials. This is due to the electron deficient **bbip**$^+$ ligand and indicates that the lowest energy excited MLCT state is localised on the **bbip**$^+$ ligand. Transforming the imidazolium structure in $[Ru(bbip)]^{3+}$ to the carbene structure in $[Ru(bbip)Ag]^{2+}$ impacts the energy of the **bbip**$^+$ ligand orbitals, which results in a shift of the first reversible reduction from −1.55 to −1.64 V. However, in the case of $[Ru(bbip)Ag]^{2+}$ additional irreversible reductions (−1.29 V) and oxidations (−0.38, +0.87) were found which are probable related to the partly irreversible decomposition of the complex, and, which hamper a direct correlation.[39] Moreover, it seems that the oxidation of Ru(II/III) at 0.87 V is overlaid by a number of irreversible redox processes.

Table 2 Selected redox potentials $E_{1/2}$ (V) of the complexes $[Ru(bbip)]^{3+}$, $[Ru(bbip)Ag]^{2+}$, and $[Ru(tbbpy)_2(phen)]^{2+}$ (*vs.* Fc/Fc$^+$ in a 0.1 M solution of Bu_4NPF_6 in dry acetonitrile under argon). Irreversible peaks are not listed for clarity

Complex	L3	L2	L1	$Ru^{II/III}$
$[Ru(bbip)]^{3+}$	−2.25	−1.98	−1.55	0.86
$[Ru(bbip)Ag]^{2+}$	−2.22	−1.96	−1.64	0.87
$[Ru(tbbpy)_2(phen)]^{2+}$ (ref. 40)	−2.25	−1.98	−1.77	0.74

Cyclic voltammograms of $[Ru(bbip)Pd]^{2+}$ and $[Ru(bbip)Rh]^{2+}$ were also measured. However, the spectra show several irreversible peaks, which make it impossible to assign the redox potentials. It is important to note that the first reduction potentials of the bbip compounds are between 130 and 220 mV more positive than observed for the **phen** based analogue as shown in Table 2. This suggests that **bbip**$^+$ ligands are easier to reduce and that therefore the lowest energy ^{3}MLCT state is based in this ligand.

Spectroelectrochemistry

In addition, spectroelectrochemical reduction and oxidation of $[Ru(bbip)]^{3+}$ were performed to establish the absorption features of its reduced and oxidised forms. Electrochemical oxidation resulted in the bleaching of the MLCT absorption (Fig. S5†), while electrochemical reduction gave rise to new bands that feature a minimum at 430 nm and maxima at 345, 470, 515 and 600 nm (Fig. S6†). Importantly, these features are reminiscent of the changes seen for **bpy**$^-$ or LMCT transitions of the Ru^{III} excited-state chromophore.[41]

Photophysical parameters

To fully understand the photophysical properties of the compounds of interest and to facilitate their utilisation as photocatalytic assemblies, detailed absorption and emission studies were carried out. The absorption and emission features of the compounds in acetonitrile are shown in Fig. 9 and 10 and are summarised in Table 3 – for dichloromethane data see Table S2 in the ESI.† The results obtained show that the absorption and emission maxima are similar to those observed for $[Ru(bpy)_3]^{2+}$, although the emission maxima show a red shift of up to 60 nm. This suggests that the emitting state is at lower energy, in agreement with the electrochemical data. The latter indicate the carbene type ligands are easier reduced than the peripheral **tbbpy** ligands and it seems likely that the emitting state may therefore be based on the carbene moiety.

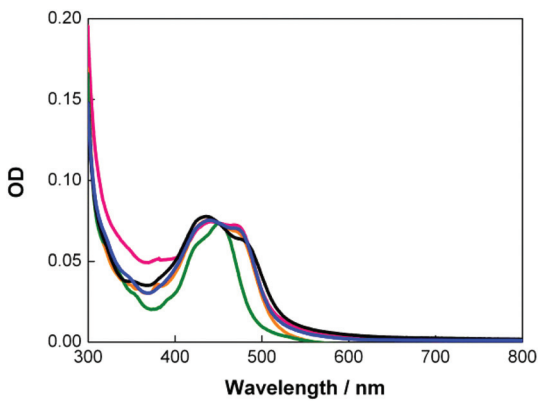

Fig. 9 Absorption spectra of $[Ru(bbip)Pd]^{2+}$ (blue), $[Ru(bbip)Ag]^{2+}$ (orange), $[Ru(bbip)]^{3+}$ (black), $[Ru(bbip)Rh]^{2+}$ (pink), and $[Ru(bpy)_3]^{2+}$ (green) in deaerated acetonitrile at room temperature with equally absorbing solutions (OD = 0.074) at 450 nm.

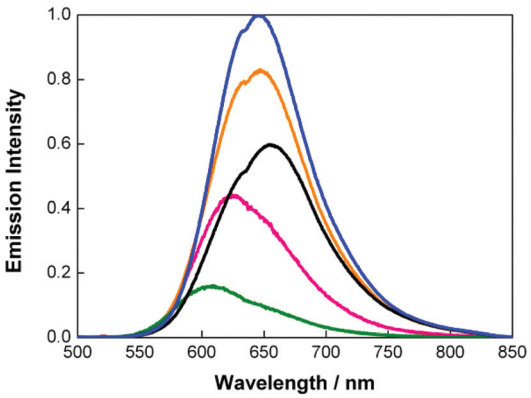

Fig. 10 Emission spectra of **[Ru(bbip)Pd]$^{2+}$** (blue), **[Ru(bbip)Ag]$^{2+}$** (orange), **[Ru(bbip)]$^{3+}$** (black), **[Ru(bbip)Rh]$^{2+}$** (pink), and **[Ru(bpy)$_3$]$^{2+}$** (green) in deaerated acetonitrile upon excitation at 450 nm at room temperature with equally absorbing solutions (OD = 0.074).

Table 3 Absorption and emission data of **[Ru(bbip)]$^{3+}$**, **[Ru(bbip)Ag]$^{2+}$**, **[Ru(bbip)Pd]$^{2+}$**, **[Ru(bbip)Rh]$^{2+}$**, and **[Ru(bpy)$_3$]$^{2+}$** measured in deaerated acetonitrile at room temperature. For further time resolved emission data see Tables S3a, S3b, S3c and S3d

Complex	$\lambda_{max,\ abs}$ [nm]	$\lambda_{sh,\ abs}$ [nm]	$\lambda_{max,\ em}$ [nm]	Φ	τ_1^a [ns]	τ_2^a [ns]
[Ru(bbip)]$^{3+}$	434	481	659	0.25	930	2142
[Ru(bbip)]$^{3+}$ + TEA	440	476	624	0.40	890	2340
[Ru(bbip)Ag]$^{2+}$	440	474	647	0.34	1447	2309
[Ru(bbip)Pd]$^{2+}$	440	475	646	0.39	717	1096
[Ru(bbip)Pd]$^{2+}$ + TEA	440	472	645	0.47	1271	1769
[Ru(bbip)Rh]$^{2+}$	440	473	625	0.17	220	2103[a]
[Ru(bpy)$_3$]$^{2+}$	451	423	607	0.06[42]	870	—
[Ru(bpy)$_3$]$^{2+}$ + TEA					850	

[a] For **[Ru(bbip)Rh]$^{2+}$** a third lifetime was observed (see ESI Table S3a).

Very notable are higher emission quantum yields, and longer ^{3}MLCT lifetimes (Fig. 9, Fig. 10, and Table 3, S3a, S3b, and Fig. S7†) compared to **[Ru(bpy)$_3$]$^{2+}$**. Striking is also the impact that the nature of the NHC bound metal exerts on the emission quantum yields. Here, the following order has been observed Pd > Ag > metal free > Rh. Very interestingly, even for the weakest emitting complex, that is, **[Ru(bbip)Rh]$^{2+}$**, a significantly higher quantum yield relative to that reported for **[Ru(bpy)$_3$]$^{2+}$** was observed. Further proof of the ^{3}MLCT nature of the emitting state is derived from singlet oxygen evolution detected in steady state emission measurements.

The emission lifetime data are more complex than expected. In dichloromethane single exponential decays are observed in aerated as well as deaerated solutions for the **[Ru(bbip)]$^{3+}$** precursor and **[Ru(bbip)Ag]$^{2+}$**. For **[Ru(bbip)Pd]$^{2+}$** and **[Ru(bbip)Rh]$^{2+}$** biexponential decays are observed (Table 3 and S3c–d†). The same is observed for aerated acetonitrile solution (Table S3b†). However in deaerated acetonitrile solution double exponential decay is observed for all compounds (Table S3a†).

At this stage this behaviour is not fully understood, but similar results were obtained for structurally related compounds.[15,29]

A potential explanation is the presence of impurities. However taking into account the detailed characterisation of the compounds with ESI-HRMS and NMR which do not show any evidence for impurities this does not look likely, although we cannot exclude this possibility totally. It is also possible that the presence of different conformers in solution is responsible, but no direct evidence for this is obtained from NMR studies. This important issue is at present under further investigation.

Taking into account the above discussion we tentative suggest that the data can be explained by the presence of two emitting states, one based on the peripheral **tbbpy** ligands and one based on the carbene moiety. The presence of two emitting states suggests a week coupling between the two states which may be surprising since they are based on the absorption spectra of the compounds expected to be close in energy. Further studies involving time resolved resonance Raman in combination of partial deuteration of the compounds are needed to better understand this behaviour.[43]

We can make a number of observations from the obtained data. Surprisingly the long components of the emission lifetimes together with the emission quantum yields are considerably larger than observed for **[Ru(bpy)$_3$]$^{2+}$** as shown in Table 3. In addition, the excited state lifetimes of the heteronuclear compounds are not quenched by the introduction of the second metal centre and are increased in some cases.[44] This may suggest week coupling between the photosensitiser and the catalytic centre and/or a strongly localised carbene excited state.

An important feature that should be central to the design of intramolecular systems is that upon excitation of the photosensitiser vectorial electron transfer to the catalytic centre is taking place *via* the bridging ligand. It is this process that makes these compounds intra- rather than intermolecular photocatalysts. Insights into such intramolecular electron transfer processes can be obtained from time resolved techniques. Femtosecond (150 fs) pump probe measurements were carried out using 480 nm excitation. In this study the photophysical properties of **[Ru(bbip)]$^{3+}$** and **[Ru(bbip)Pd]$^{2+}$** were investigated. The results gathered for **[Ru(bbip)]$^{3+}$** are in line with those obtained for similar polypyridyl compounds and indicate rapid intersystem crossing of the initially populated ^{1}MLCT excited state. The population of the correspondingly ^{3}MLCT excited state from the associated singlet state for **[Ru(bbip)]$^{3+}$** is about 150 fs similar to that obtained for **[Ru(bpy)$_3$]$^{2+}$** (~100–300 fs)[41] (Fig. 11; lower part). Characteristic features observed for **[Ru(bbip)]$^{3+}$** include minima and maxima at 443 and 560 nm, respectively, and these compare well to those of **[Ru(bpy)$_3$]$^{2+}$** (ref. 41) (Fig. 11, upper part). Fig. S8† shows differential absorption changes during the 8 ns timescale of our femtosecond instrumentation showed no appreciable decay. To further investigate this feature pump probe measurements on the nanosecond timescale were

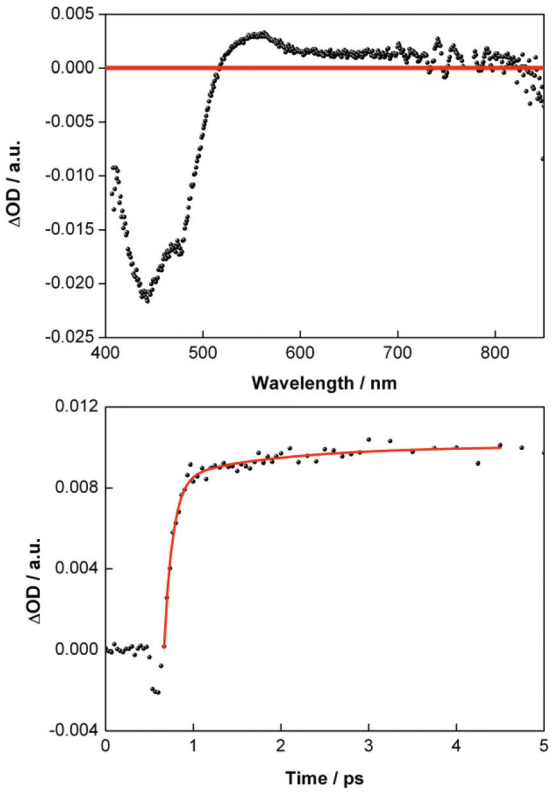

Fig. 11 Upper part: Differential absorption spectrum (visible) obtained upon femtosecond flash photolysis (480 nm) of **[Ru(bbip)]**$^{3+}$ in deaerated acetonitrile with a time delay of 1 ps. Lower part: Time absorption profile at 560 nm, monitoring the intersystem crossing of the ^{1}MLCT state of **[Ru(bbip)]**$^{3+}$ into the ^{3}MLCT state.

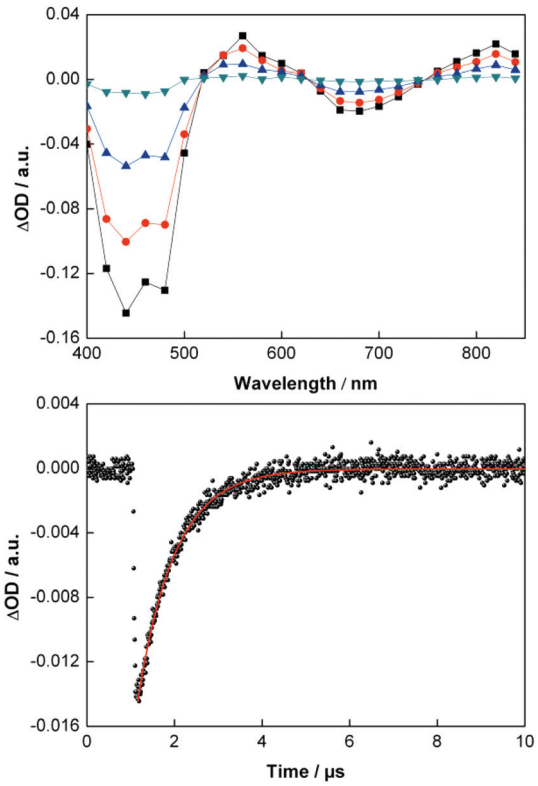

Fig. 12 Upper part: Differential absorption spectrum (visible) obtained upon nanosecond flash photolysis (532 nm) of **[Ru(bbip)]**$^{3+}$ in deaerated acetonitrile with time delays of 0.2 μs (black), 0.5 μs (red), 1.0 μs (blue) and 2.5 μs (green). Lower part: Time absorption profile at 680 nm, monitoring the decay of ^{3}MLCT state of **[Ru(bbip)]**$^{3+}$.

carried out. A notable difference in the spectra of **[Ru(bbip)]**$^{3+}$ relative to the aforementioned spectra on the shorter time scale is that the region from 610 to 780 nm is masked by ^{3}MLCT centred emission. However, in the differential absorption spectra of **[Ru(bbip)]**$^{3+}$, a minimum was observed at 440 nm as well as maxima at 560 and 820 nm (Fig. 12, upper part) correlating either with a transition that is centred on a reduced ligand or with a ligand-to-metal charge-transfer (LMCT) transition to the formally oxidised Ru(III) ion of the ^{3}MLCT state.[41] In the absence of molecular oxygen, all ^{3}MLCT excited state features decay, in agreement with the time-resolved emission experiments, quantitatively back to the ground state following the same kinetics, which indicates that the ^{3}MLCT decay and the ground state recovery go hand in hand.[45] At delay times beyond 20 μs, no residual transitions neither in the form of bleaching nor positive absorption remain. From the decay profiles ^{3}MLCT excited state lifetimes were determined to be around 1000 ns. Similar results were obtained by investigating **[Ru(bbip)Pd]**$^{2+}$ (Fig. S9a, S9b, S10a, and S10b†) with related transitions; a minimum at 480 nm and two maxima at 560 and 820 nm these have been assigned in the same spectroscopic features as discussed for **[Ru(bbip)]**$^{3+}$.[41] In contrast, the region from 600 to 760 nm reflects the ^{3}MLCT centred emission.

The emission properties of **[Ru(bbip)]**$^{3+}$ and **[Ru(bbip)Pd]**$^{2+}$ in the presence of various amounts of triethylamine (TEA) a known sacrificial electron donor, were probed. The addition of TEA caused no appreciable changes to the absorption spectra regardless of the concentration of the quencher. On the other hand, the ^{3}MLCT emission spectra reveal an intensification by a factor of 1.62 and 1.21 for **[Ru(bbip)]**$^{3+}$ and **[Ru(bbip)Pd]**$^{2+}$, respectively, rather than a quenching. Furthermore a blue shift from 659 to 624 nm is observed (Fig. S11,† Table 3). These data suggest that TEA interacts strongly with both **[Ru(bbip)]**$^{3+}$ and **[Ru(bbip)Pd]**$^{2+}$ by stabilizing the emissive ^{3}MLCT excited state (Table 3 and S3a†). A striking observation is that in the presence of 0.108 M TEA the emission lifetimes of the **[Ru(bbip)]**$^{3+}$ and the corresponding Pd compounds increase rather than decrease as would be expected if reductive quenching was taking place. For **[Ru(bpy)$_3$]**$^{2+}$ a small decrease was observed indicating the rather weak ability of TEA to quench most ruthenium polypyridyl complexes. The observed increase in excited state lifetimes for the carbene compounds may be due to preferential solvation of the complexes by TEA or possibly by reductive quenching forming a long-lived reduced ruthenium complex, see below. Hereby, **tbbpy** and **bbip**$^{+}$ ligands are involved. In the presence of TEA, the relative amplitudes of the longer lifetime (about 2 μs) increases,

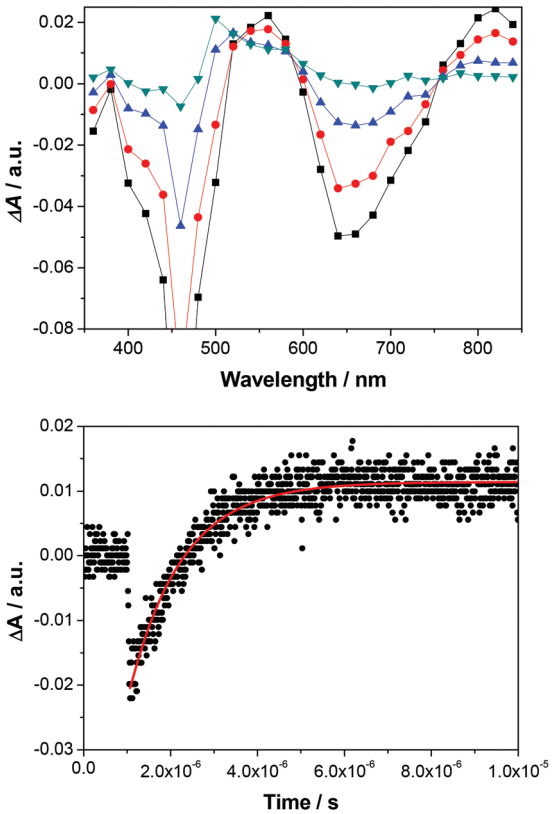

Fig. 13 Upper part: Differential absorption spectra (visible) obtained upon nanosecond flash photolysis (532 nm) of **[Ru(bbip)Pd]**$^{2+}$ with 3 equivalents of TEA in deaerated acetonitrile with time delays of 0.2 μs (black), 0.8 μs (red), 2.0 μs (blue) and 5.0 μs (green). Lower part: Time absorption profile at 500 nm, monitoring the **[Ru(bbip)Pd]**$^{+}$.

while that of the shorter one (about 1 μs) decreases (Table S3a†).§

As such, the emission enhancement might be due to the transition to the bridging ligand, while a potential quenching is due to the transition to **tbbpy**. This is further corroborated by the decrease of the shorter lifetime from 930 to 890 ns and the increase of the longer lifetime from 2142 to 2340 ns, for instance, in the case of **[Ru(bbip)]**$^{3+}$ (Table S3a†).

Additionally, in nanosecond pump probe measurements the decay kinetics of the ^{3}MLCT centred emission, which spans from 610 to 780 nm, shows a pronounced effect upon addition of TEA (Fig. 13 and S12†).

In the case of **[Ru(bbip)]**$^{3+}$ the lifetime increases from 1018 to 1551 ns in the absence and presence of 0.108 M TEA. This correlates to an increase by a factor of 1.52. A similar observation was recently made for another ruthenium polypyridyl complex.[46] Commencing with the decay of the excited state a transient evolves that exhibits a minimum at 460 nm and a maximum at 500 nm. Notable is also the broadening of the maximum (Fig. 12 and S12a†). In line with our spectroelectrochemical investigations – *vide supra* – and previous studies on **[Ru(bpy)$_3$]**$^{2+}$ (ref. 47 and 48) we ascribe this observed process to the reductive quenching of an excited state. As a matter of fact the reduced complexes **[Ru(bbip)]**$^{2+}$ and **[Ru(bbip)Pd]**$^{+}$ and the oxidized TEA, *i.e.* the radical cation are formed. Spectroscopic evidence for the reduction is the 500 nm maximum, while the broadening around 475 nm refers to the oxidation of TEA (Fig. S12a†).[47] Based on this analysis we could determine the lifetime of the reduced complex **[Ru(bbip)]**$^{2+}$. Within the time window of 9 ms a lifetime of 3.3 ms was derived from the 500 nm fingerprint of **[Ru(bbip)]**$^{2+}$ (Fig. S12b†).

§ Alternative explanations for this phenomenon could be the appearance of two different conformers in solution due to the benzyl groups attached to the **bbip**$^{+}$ ligand, deprotonation events for the imidazolium C–H function in the excited state and ligand rearrangements at the carbene bound metal complexes.

Catalytic activity

Based on these results all the new ruthenium compounds were tested as photocatalysts for hydrogen formation. Irradiation with visible light (λ = 470 nm, suitable to excite into the MLCT-band) was carried out under identical conditions in a water–triethylamine–acetonitrile (2 : 6 : 12/v : v : v) mixture (Fig. 14). The hydrogen formed was quantified by GC-TCD. The highest turnover numbers (TONs) were observed for **[Ru(bbip)Pd]**$^{2+}$ with 36 turnovers after 5 hours at a constant frequency of 7 turnovers per hour. The catalytic activity with respect to TON and TOF is independent on the catalyst concentration, which was varied between 250 and 10 μM. **[Ru(bbip)Rh]**$^{2+}$ reaches a lower TON of 16. Surprisingly, even the silver complex **[Ru(bbip)Ag]**$^{2+}$ shows some catalytic activity with 4 turnovers in five hours. As expected, the control experiments with the mononuclear **[Ru(bbip)]**$^{3+}$ complex show no hydrogen production.

In contrast to other intramolecular photoredox catalysts, like [(tbbpy)$_2$Ru(tpphz)PdCl$_2$]$^{2+}$,[9] no induction period is observed for any of the new complexes, since hydrogen is detected already after a few minutes of irradiation. Several important conclusions can be drawn from these observations. Firstly, **[Ru(bbip)]**$^{3+}$ serves as a photosensitizer for the three different catalytic centres. Secondly, the lack of an induction phase, the concentration independence of catalytic activity,

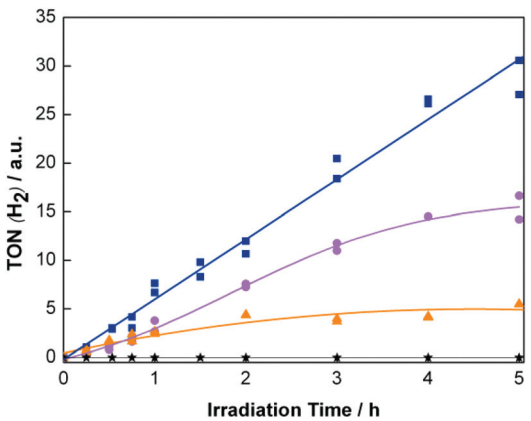

Fig. 14 TON of hydrogen production with a 0.25 mM solution of **[Ru(bbip)]**$^{3+}$ (black), **[Ru(bbip)Ag]**$^{2+}$ (orange), **[Ru(bbip)Rh]**$^{2+}$ (purple) and **[Ru(bbip)Pd]**$^{2+}$ (blue) in ACN–H_2O–TEA during the course of five hours.

and the constant turn over frequency, especially for **[Ru(bbip)Pd]$^{2+}$**, support an increased chemical stability of the whole photoactive catalyst by using NHC-bridging ligands. The influence of potential dimeric structures in the catalytic mixtures is currently under investigations.

To investigate whether the [Ru(bbip)M]$^{2+}$ complexes are stable during irradiation DLS measurements were performed under catalytic conditions. For **[Ru(bbip)Ag]$^{2+}$** a linear correlation between particle growth and irradiation time was observed (Fig. S13†). A possible explanation for this could be the known formation of complex silver halogenido anions during synthesis[49,50] or the formation of silver particles over the known photographic effect. Since DLS is not a quantitative method of analysis very small amounts of impurities of a silver halogenide may generate over the known photographic effect a detectible silver particle. Similar experiments were performed for **[Ru(bbip)Pd]$^{2+}$**. However, no clear conclusion could be drawn from the obtained results. A potential explanation may be the presence of silver based impurities which may occur also during the synthesis of **[Ru(bbip)Pd]$^{2+}$** and **[Ru(bbip)Rh]$^{2+}$** alternative methods of investigation such as TEM may be needed. Further investigations into this direction are in progress.

Experimental

Used chemicals

All chemicals were of reagent grade and were used without any further purification. Where necessary all manipulations were carried out by using Schlenk techniques under argon atmosphere. The synthesis of all compounds is described in the ESI† in detail. All measurements were performed under aerobic conditions at room temperature unless stated otherwise. The solvents used for all investigations were purified with a state of the art solvent purification system for organometallic reagents, if not stated otherwise. TEA was distilled over CaH_2 under argon for purification.

Steady state UV/vis absorption spectroscopy

Steady state absorption spectra were obtained using a Perkin Elmer Lambda2 UV/vis two-beam spectrophotometer using a slit width of 2 nm and a scan rate of 480 nm min^{-1}. All spectra were recorded using a quartz glass cuvette of 10 × 10 mm.

Steady state emission spectroscopy

Steady state emission spectra were recorded using a Horiba Jobin Yvon FluoroMax-3 spectrometer using a slit width of 2 nm for excitation and emission and an integration time of 0.5 s. The studies were performed in a 10 × 10 mm quartz glass cuvette. The emission spectra are corrected for light power by the spectrometer. However, regarding the detector sensitivity they are not corrected. Emission quantum yields are derived from a comparison of the integrated area of emission to the reference compound **[Ru(bpy)$_3$]$^{2+}$** (Φ = 0.06 in ACN[51]) detected at equally absorbing solution at the excitation wavelength of 450 nm.

Time resolved emission studies

Emission lifetimes were determined *via* time correlated single photon counting (TCSPC) on a Horiba Jobin Yvon FlouroLog3 emission spectrometer with a Hamamatsu MCP photomultiplier (R3809U-58). For excitation a laser diode (NanoLED-405L, 403 nm, pulse width ≤200 ps, maximum of repetition rate 100 kHz) was used. All measurements were performed in a 10 × 10 mm quartz glass cuvette.

Electrochemistry

Electrochemical data were obtained by cyclic voltammetry using a conventional single-compartment three-electrode cell arrangement in combination with a potentiostat "AUTOLAB®, eco chemie" or Princeton Applied Research PARSTAT® 2273. As auxiliary and reference electrode two Pt wires were used; working electrode: glassy carbon. The measurements were carried out in anhydrous and argon saturated acetonitrile. Tetrabutylammonium hexafluorophosphate ($TBAPF_6$ = 0.1 M) was used as supporting electrolyte at ambient temperature (20 (±5) °C). All potentials are referenced to the internal standard ferrocene/ferrocenium ($E_{(Fc/Fc+)}$ = 0.00 V). Therefore, the redox potential $E_{(Fc/Fc+)}$ was shifted from 0.40 V *versus* SCE as measured in the CV-set up to 0.00 V.

Spectroelectrochemistry

Spectroelectrochemical experiments were carried out using a HEKA Elektronik Potentiostat/Galvanostat PG284 and a SPECORD S600 Analytic Jena spectrophotometer. The measurements were performed in a homemade three neck cell ($d \sim 0.3$ cm) with a platinum gauze (working electrode), a platinum wire (counter electrode) *versus* a silver wire (pseudo reference electrode) under argon atmosphere. Tetrabutylammonium hexafluorophosphate ($TBAPF_6$ = 0.2 M) was used as supporting electrolyte. All potentials are referenced to ferrocene/ferrocenium ($E_{(Fc/Fc+)}$ = 0.00 V).

Femtosecond transient absorption spectroscopy

Femtosecond transient absorption studies were performed with an amplified Ti/sapphire laser system (Model CPA 2101, Clark-MXR Inc. – output: 775 nm, 1 kHz and 150 fs pulse width) in the TAPPS – Transient Absorption Pump/Probe System – Helios from Ultrafast Systems. That is referred to a two-beam setup where the pump pulse of 480 nm and 200 nJ, generated out of a NOPA – noncollinear optical parametrical amplifier, Clark MRX Inc. – is used as excitation source for transient species and the delay of the probe pulse is exactly controlled by an optical delay rail of 3.3 ns. As probe beam (white light continuum), a small fraction of 775 nm pulses stemming from the CPA laser system was focused by a 50 mm lens into a 3 mm thick sapphire disc. Finally, the changes in optical density (ΔA) were measured against the wavelength in both visible and near-infrared regions. The transient spectra were recorded in a 10 × 2 mm quartz glass cuvette.

Nanosecond transient absorption spectroscopy

For nanosecond transient absorption experiments the samples were excited with the output of the second harmonic (532 nm) coming from a Nd:YAG laser. Moreover, pulse widths of less than 5 ns with energies of up to 7 mJ were selected. The optical detection was based on a pulsed Xenon lamp, a monochromator, a photomultiplier tube or a fast silicon photodiode with a 1 GHz amplification and a 500 MHz digital oscilloscope. The laser power of every laser pulse was registered using a bypath with a fast silicon photodiode. The experiments were performed in a 10 × 5 mm quartz glass cuvette.

Mass spectrometry

The ESI experiments discussed above (Fig. 5 and the data shown in Fig. S3†) were performed with an Esquire 6000 (Bruker) ion trap mass spectrometer. High-resolution mass spectrometry (HRMS) was performed using a Fourier Transform Ion Cyclotron Resonance (FT-ICR) mass spectrometer solariX (Bruker Daltonik GmbH, Bremen, Germany) equipped with a 7.0 T superconducting magnet and interfaced to an Apollo II Dual ESI/MALDI source. As solvents 0.1 M HCOOH. aq–MeOH (9 : 1/v : v) (**ip**), methanol (**bip**, **bbip**$^+$, **[Ru(bbip)]**$^{2+}$ and **[Ru(bbip)]**$^{3+}$) and acetonitrile (**[Ru(ip)]**$^{2+}$, **[Ru(bbip)Ag]**$^{2+}$, **[Ru(bbip)Pd]**$^{2+}$ and **[Ru(bbip)Rh]**$^{2+}$) were used.

NMR-experiments

The NMR spectra were recorded on a Lambda/Eclipse 400 (Jeol; 400 MHz) and an AVANCE 400 (Bruker; 400 MHz).

Crystal-structure analyses

The intensity data for the compounds **ip**, **bip**, **bbip**$^+$, **[Ru(ip)]**$^{2+}$, **[Ru(bip)]**$^{2+}$ and **[Ru(bbip)]**$^{3+}$ were collected on a Bruker-Nonius KappaCCD diffractometer, using graphite-monochromated Mo-K_α radiation (λ = 0.71069 Å, graphite monochromator) at −140(2) °C. Data were corrected for Lorentz, polarization effects, and for absorption effects.[52,53] ¶ The structures were solved by direct methods (SHELXS) and refined by full-matrix least squares techniques against F_o^2 (SHELXL-97). The hydrogen atoms were included at calculated positions with fixed thermal parameters. All nonhydrogen atoms were refined anisotropically.[54] XP (SIEMENS Analytical X-ray Instruments, Inc.) was used for structure representations. Intensity data for **[Ru(bbip)Ag]**$^{2+}$ were collected on a Bruker-Nonius KappaCCD diffractometer using graphite-monochromated Mo-K_α radiation (λ = 0.71073 Å). Data were corrected for Lorentz and polarization effects; absorption was taken into account on a semi-empirical basis using multiple scans (SADABS 2.10‖). The structure was solved by direct methods and refined by full-matrix least-squares techniques on F^2 (SHELXLTL 6.12[54]). The two chloride anions were distributed over three different crystallographic sites with one site being occupied by 100% and the other two by 50% only. The compound crystallized with a total of 6.54 molecules of $CHCl_3$ and 1.27 molecules of THF per formula unit. Some of the $CHCl_3$ molecules were disordered and shared their crystallographic sites with THF molecules. The following site occupancies for the disordered solvent molecules were obtained: 53.3(6)% for C500–Cl53, 38.3(6)% for C600–Cl63, 42.3(8)% for C610–Cl66, 29.3(7)% for C700–Cl73, 39.5(7)% for C800–Cl83, 50% for C900–Cl93, 70.7(7)% for O600–C604 and 56.8(11)% for O900–C904. SAME, SIMU, and ISOR restraints were applied in the refinement of the disorder. H atom positions of the water molecule were derived from a difference Fourier and were not further refined. All other hydrogen atoms were placed in positions of idealized geometry. The isotropic displacement parameters of all H atoms were tied to the equivalent isotropic displacement parameter of their corresponding carrier atom by a factor of 1.2 or 1.5. CCDC 893729 (for **ip**), CCDC 893730 (for **bip**), CCDC 893731 (for **bbip**$^+$), CCDC 893732 (for **[Ru(ip)]**$^{2+}$), CCDC 893733 (for **[Ru(bip)]**$^{2+}$), CCDC 765499 (for **[Ru(bbip)]**$^{3+}$), and CCDC 796734 (for **[Ru(bip)Ag]**$^{2+}$) contain the supplementary crystallographic data for this paper.

Catalysis experiments

The photohydrogen production experiments were carried out using a home-built air-cooling apparatus for maintaining room temperature (22 °C) and constant irradiation of the sample. 5 ml GC vials (diameter = 13 mm, VWR) with a known headspace of 3 ml and a headspace/solution ratio of 3/2 were used as reaction vessels. Directly before the irradiation experiments, fresh stock solutions of the respective samples with solvent mixtures of acetonitrile, triethylamine and water in a 6 : 3 : 1 ratio (v : v : v) and with the desired concentrations of ruthenium complex (10 μM, 50 μM, 100 μM and 250 μM) were prepared in the dark. Then, the required number of GC vials was charged in the dark and under nitrogen atmosphere. Subsequently, the samples were irradiated with a LED-array (54 LEDs, exit angle 15°, luminous intensity 14.0 cd each, from Innotas Elektronik GmbH, Zittau, Germany) at a wavelength of (λ = 470 nm, suitable to excite in the MLCT-band). After the irradiation, 100 μl gas samples were drawn from the headspace and injected immediately into the GC apparatus. The concentration of evolved hydrogen was quantified by headspace GC on a GCMS-QP2010S chromatograph from Shimadzu, with a thermal conductivity detector and a Rtx®-5MS (Fused Silica) column (length 30 m, 0.25 mm inner diameter, layer thickness 0.25 μm) with nitrogen as carrier gas (purity 99.999%) an oven temperature of 70 °C, a flow rate of 22.5 ml min^{-1}, a detector temp. of 220 °C, and a pressure of 102.1 kPa were used. The GC was calibrated by mixing different volumes of pure hydrogen (0–100%) together with nitrogen into a Schlenk vessel. The obtained signal (retention time for H_2, t_R = 1.95 min) was plotted against the calibration curve and multiplied accordingly to receive the total produced hydrogen content in the headspace. Irradiation experiments and hydrogen measurements were repeated several times for each reaction time (between 2 and 12 h) and catalyst concentration.

¶COLLECT, Data Collection Software; Nonius B.V., Netherlands, 1998.
‖ *SADABS 2.10*, Bruker-AXS Inc., 2002, Madison, WI, U.S.A.

Particle size measurement

The DLS-measurements were obtained using a Delsa Nano C Particle Analyzer from Beckman Coulter. As light source dual 30 mW laser diodes with a wavelength of 658 nm were used. All measurements were performed at 25 °C. For the viscosity a value of 0.58 mPa s with a failure range of ±0.10 mPa s and for the refractive index a value of 1.3648 determined for the catalytic mixture. All size calculations were done with standard calculation methods. All measurements were performed applying 10 × 10 mm quartz SUPRASIL inert cuvettes from Hellma. All experiments were repeated with three identical solutions to ensure the reproducibility of the data. All solvents were degassed with nitrogen before use. The catalytic mixtures consisted of 1.2 ml acetonitrile (with the photo catalyst), 0.6 ml Et_3N and 0.2 ml water. The final concentration of the photo catalyst in the catalytic solution was 50 μM. This mixture was filled into the cuvettes through a syringe filter (pore size 0.2 μm) under inert conditions. All solutions were measured immediately. In the beginning every solution was investigated without irradiation. Each experiment was repeated several times. Between the measurements the solutions were irradiated with led-arrays (λ = 470 nm).

Conclusions

A novel NN-NHC-bridging ligand was designed and used to synthesize a new type of photoredox active metal complexes, where the second metal centre is bound by the NHC-carbene unit. The full characterization including X-ray structural data for the heterodinuclear **[Ru(bbip)Ag]$^{2+}$** complex unambiguously confirms the presence of the carbene substructure. The photophysics showed absorption and emission features typical for light harvesting ruthenium complexes. Most relevant for photocatalytic application are the observed, dual emission, high quantum yields, and long lifetimes for the emissive and non-emissive dark ^{3}MLCT in **[Ru(bbip)]$^{3+}$** and **[Ru(bbip)Pd]$^{2+}$**. Finally, the photocatalytic investigations of hydrogen formation from water in the presence of a sacrificial electron donor showed several features reminiscent of stable catalysts like constant turnover frequencies, independence of activity on concentration of the catalyst and mainly the absence of an induction phase.

This evidence provides the opportunity to further optimize the catalytic performance of these systems for instance along the lines described for the $[(tbbpy)_2Ru(tpphz)PdCl_2][PF_6]_2$.[9] All aspects observed so far suggest a high stability of the new NN-NHC bridged heterodinuclear complexes, which support the assumption that the NHC-donor set has a favourable influence on catalytic centres. Further investigations aimed at improving catalytic activity by optimizing the conditions like solvent composition and water concentration are under way. This new type of photoredox active dinuclear complexes bridged by a more stabilizing NN-NHC ligand showed a promising way for further synthesis of photoactive catalysts.

Acknowledgements

This work was funded by a promotion scholarship of the Carl-Zeiss-Stiftung, the Elitenetzwerk Bayern, the graduate school molecular science FAU Erlangen Nuremberg, the DFG, the GRK 1626, the SFB 583 and Solar Technologies Go Hybrid. We would like to acknowledge the work of team of Dr W. Poppitz at the FSU-Jena for additional mass spectroscopic measurements.

Notes and references

1 N. Armaroli and V. Balzani, *Angew. Chem., Int. Ed.*, 2007, **46**, 52–66.
2 W. J. Youngblood, S.-H. A. Lee, K. Maeda and T. E. Mallouk, *Acc. Chem. Res.*, 2009, **42**, 1966–1973.
3 E. Amouyal, *Sol. Energy Mater. Sol. Cells*, 1995, **38**, 249–276.
4 J.-M. Lehn and J.-P. Sauvage, *Nouv. J. Chim.*, 1977, **1**, 449–451.
5 L. Sun, L. Hammarström, B. Åkermark and S. Styring, *Chem. Soc. Rev.*, 2001, **30**, 36–49.
6 A. Inagaki and M. Akita, *Coord. Chem. Rev.*, 2010, **254**, 1220–1239.
7 M. Schulz, M. Karnahl, M. Schwalbe and J. G. Vos, *Coord. Chem. Rev.*, 2012, **256**, 1682–1705.
8 S. Rau, B. Schäfer, D. Gleich, E. Anders, M. Rudolph, M. Friedrich, H. Görls, W. Henry and J. G. Vos, *Angew. Chem., Int. Ed.*, 2006, **45**, 6215–6218.
9 S. Tschierlei, M. Karnahl, M. Presselt, B. Dietzek, J. Guthmuller, L. González, M. Schmitt, S. Rau and J. Popp, *Angew. Chem., Int. Ed.*, 2010, **49**, 3981–3984.
10 T. A. White, B. N. Whitaker and K. J. Brewer, *J. Am. Chem. Soc.*, 2011, **133**, 15332–15334.
11 P. Lei, M. Hedlund, R. Lomoth, H. Rensmo, O. Johansson and L. Hammarström, *J. Am. Chem. Soc.*, 2008, **130**, 26–27.
12 P. Du, J. Schneider, F. Li, W. Zhao, U. Patel, F. N. Castellano and R. Eisenberg, *J. Am. Chem. Soc.*, 2008, **130**, 5056–5058.
13 K. Yamauchi, S. Masaoka and K. Sakai, *J. Am. Chem. Soc.*, 2009, **131**, 8404–8406.
14 R. Jackstell, G. M. Andreu, A. Frisch, K. Selvakumar, A. Zapf, H. Klein, A. Spannenberg, D. Röttger, O. Briel, R. Karch and M. Beller, *Angew. Chem., Int. Ed.*, 2002, **41**, 986–989.
15 H.-J. Park and Y. K. Chung, *Inorg. Chim. Acta*, 2012, **391**, 105–113.
16 H.-J. Park, K. Kim and Y. K. Chung, *Inorg. Chim. Acta*, 2014, **410**, 214–220.
17 T. D. Pilz, *Development of Novel Catalysts for the Photocatalytic Hydrogen Formation*, Friedrich-Schiller-Universität, Jena, 2011.
18 J.-Z. Wu, B. Ye, L. Wang, L.-N. Ji, J.-Y. Zhou, R.-H. Li and Z.-Y. Zhou, *J. Chem. Soc., Dalton Trans.*, 1997, 1395–1401.
19 L. Benhamou, E. Chardon, G. Lavigne, S. Bellemin-Laponnaz and V. César, *Chem. Rev.*, 2011, **111**, 2705–2733.
20 A. J. Arduengo, J. R. Goerlich and W. J. Marshall, *J. Am. Chem. Soc.*, 1995, **117**, 11027–11028.

21 V. P. W. Böhm and W. A. Herrmann, *Angew. Chem., Int. Ed.*, 2000, **39**, 4036–4038.
22 Y. Yamaguchi, T. Kashiwabara, K. Ogata, Y. Miura, Y. Nakamura, K. Kobayashi and T. Ito, *Chem. Commun.*, 2004, 2160–2161.
23 H. M. J. Wang and I. J. B. Lin, *Organometallics*, 1998, **17**, 972–975.
24 D. Rieger, S. D. Lotz, U. Kernbach, S. Schröder, C. André and W. P. Fehlhammer, *Inorg. Chim. Acta*, 1994, **222**, 275–290.
25 N. G. Tsierkezos, M. Diefenbach, J. Roithová, D. Schröder and H. Schwarz, *Inorg. Chem.*, 2005, **44**, 4969–4978.
26 P. M. Lalli, T. S. Rodrigues, A. M. Arouca, M. N. Eberlin and B. A. D. Neto, *RSC Adv.*, 2012, **2**, 3201–3203.
27 J. Li, W. Wei, L. C. Nye, P. S. Schulz, P. Wasserscheid, I. Ivanović-Burmazović and T. Drewello, *Phys. Chem. Chem. Phys.*, 2012, **14**, 5115–5121.
28 S. Rau, R. Fischer, M. Jäger, B. Schäfer, S. Meyer, G. Kreisel, H. Görls, M. Rudolf, W. Henry and J. G. Vos, *Eur. J. Inorg. Chem.*, 2004, **2004**, 2001–2003.
29 H.-J. Park, W. Kim, W. Choi and Y. K. Chung, *New J. Chem.*, 2013, **37**, 3174–3182.
30 R. Kishore and S. K. Das, *J. Mol. Struct.*, 2013, **1053**, 38–47.
31 C. L. Winn, F. Guillen, J. Pytkowicz, S. Roland, P. Mangeney and A. Alexakis, *J. Organomet. Chem.*, 2005, **690**, 5672–5695.
32 J. Pytkowicz, S. Roland and P. Mangeney, *J. Organomet. Chem.*, 2001, **631**, 157–163.
33 J. Berding, H. Kooijman, A. L. Spek and E. Bouwman, *J. Organomet. Chem.*, 2009, **694**, 2217–2221.
34 D. Tapu, D. A. Dixon and C. Roe, *Chem. Rev.*, 2009, **109**, 3385–3407.
35 F. Ullah, M. K. Kindermann, P. G. Jones and J. Heinicke, *Organometallics*, 2009, **28**, 2441–2449.
36 A. R. Chianese, X. Li, M. C. Janzen, J. W. Faller and R. H. Crabtree, *Organometallics*, 2003, **22**, 1663–1667.
37 N. Marion and S. P. Nolan, *Acc. Chem. Res.*, 2008, **41**, 1440–1449.
38 P. V. Kumar, W.-S. Lin, J.-S. Shen, D. Nandi and H. M. Lee, *Organometallics*, 2011, **30**, 5160–5169.
39 B. Liu, Y. Zhang, D. Xu and W. Chen, *Chem. Commun.*, 2011, **47**, 2883–2885.
40 B. Schäfer, H. Görls, S. Meyer, W. Henry, J. G. Vos and S. Rau, *Eur. J. Inorg. Chem.*, 2007, **2007**, 4056–4063.
41 N. H. Damrauer, G. Cerullo, A. Yeh, T. R. Boussie, C. V. Shank and J. K. McCusker, *Science*, 1997, **275**, 54–57.
42 A. C. Benniston, A. Harriman, F. M. Romero and R. Ziessel, *Dalton Trans.*, 2004, 1233–1238.
43 W. Henry, C. G. Coates, C. Brady, K. L. Ronayne, P. Matousek, M. Towrie, S. W. Botchway, A. W. Parker, J. G. Vos, W. R. Browne and J. J. McGarvey, *J. Phys. Chem. A*, 2008, **112**, 4537–4544.
44 K. Sakai, H. Ozawa, H. Yamada, T. Tsubomura, M. Hara, A. Higuchi and M.-A. Haga, *Dalton Trans.*, 2006, 3300–3305.
45 Q. Sun, S. Mosquera-Vazquez, L. M. L. Daku, L. Guénée, H. a. Goodwin, E. Vauthey and A. Hauser, *J. Am. Chem. Soc.*, 2013, **135**, 13660–13663.
46 R. Staehle, S. Losse, M. R. Filipovic, I. Burmazović, J. G. Vos and S. Rau, *ChemPlusChem*, 2014, accepted.
47 C. R. Rivarola, S. G. Bertolotti and C. M. Previtali, *Photochem. Photobiol.*, 2006, **82**, 213–218.
48 O. Ishitani, K. Ishii, S. Yanagida, C. Pac, T. Ohno and A. Yoshimura, *Chem. Lett.*, 1989, **18**, 217–220.
49 W. Huang, R. Zhang, G. Zou, J. Tang and J. Sun, *J. Organomet. Chem.*, 2007, **692**, 3804–3809.
50 X. Hu, Y. Tang, P. Gantzel and K. Meyer, *Organometallics*, 2003, **22**, 612–614.
51 A. Juris, V. Balzani, F. Barigelletti, S. Campagna, P. Belser and A. Von Zelewsky, *Coord. Chem. Rev.*, 1988, **84**, 85–277.
52 Z. Otwinowski and W. Minor, in *Methods Enzymol*, ed. C. W. Carter Jr., Elsevier Inc., 1997, pp. 307–326.
53 R. H. Blessing, *J. Appl. Crystallogr.*, 1997, **30**, 421–426.
54 G. M. Sheldrick, *Acta Crystallogr., Sect. A: Found. Crystallogr.*, 2008, **64**, 112–122.